Earth, Planets and Space

FULL PAPER Open Access

Small-scale scattering heterogeneities beneath the northern Tien Shan from the teleseismic P wavefield

Xiaolong Ma and Zongying Huang*

Abstract

In order to investigate the small-scale scattering heterogeneities underneath the northern Tien Shan, we analyze the P wavefield from teleseismic events. By using the teleseismic fluctuation method, we separate the total wavefield into coherent and fluctuating parts in the frequency band of 0.1–8.0 Hz. Subsequently, we investigate the scattering characteristics by analyzing the frequency-dependent intensities of the coherent and fluctuating wavefield between 0.3 and 2.5 Hz. We further constrain the velocity perturbations and correlation lengths by modeling the P-wave coda envelope with the Monte Carlo simulation. Strong scattering heterogeneities are revealed beneath the northern Tien Shan. The preferred scattering model can be described as a ~ 55- to 130-km-thick randomly heterogeneous layer with velocity perturbations of 6–9% and correlation lengths on the order of 0.4 km. We attribute these small-scale scatterers to isolated melt pockets from the upwelling hot mantle materials.

Keywords: P-wave coda, Small-scale scattering heterogeneities, Random media, Monte Carlo simulation, Melt pockets, Upwelling mantle materials

Introduction

Most seismic studies of Earth's velocity structure depend on the observations of travel times and waveforms of direct seismic waves (Shearer 2015). The analysis of these direct waves can in general resolve large-scale heterogeneous structures in the Earth. For example, tomographic and waveform modeling studies have revealed seismic heterogeneities on the scale of hundreds or tens of kilometers (e.g., Tkalčić et al. 2015; French and Romanowicz 2015; Lai et al. 2019; Ma et al. 2019). However, the spatial resolution of such analysis is usually limited in resolving smaller-scale heterogeneities, such as scattering media, due to the dominant wavelengths used. To solve this problem, coda waves are usually analyzed for characterizing much finer structures in a statistical sense based on the random medium approach (e.g., Aki 1969; Wu and Aki 1985). Using such an approach, the average statistical properties of the random heterogeneities can be obtained.

Seismic coda is generally defined as a tail of randomly fluctuating waves arriving after deterministic phases over an extended time interval in a seismogram (Sato et al. 2012). The coda waves are attributed to the superimposition of waves scattered off small-scale structural heterogeneities in various directions inside the Earth (Aki and Chouet 1975). Analysis of coda waves can thus lead to detailed views of seismic structure and provide valuable information on the dynamics and evolution of the Earth (e.g., Kubanza et al. 2006). To explore the stochastic properties of these small-scale heterogeneities in the crust and upper mantle, for several decades, direct and coda waves propagating in the random media have been intensively studied based on both theoretical and numerical methods (e.g., Aki 1973; Scherbaum and Sato 1991; Gusev and Abubakirov 1999; Kubanza et al. 2007;

*Correspondence: zyhuang@gig.ac.cn
State Key Laboratory of Isotope Geochemistry, Guangzhou Institute of Geochemistry, Chinese Academy of Sciences, Guangzhou 510640, China

Takahashi et al. 2009; Carcolé and Sato 2010; Yoshimoto et al. 2015; Eulenfeld and Wegler 2017; Emoto and Sato 2018).

For example, the radiative transfer theory (RTT), also known as energy transport theory, has often been used for studying seismogram envelopes and scattering of wave intensity (e.g., Zeng et al. 1991; Wegler et al. 2006; Sato and Emoto 2018) as well as intrinsic and scattering attenuation (e.g., Wu 1985; Gaebler et al. 2015; Wang and Shearer 2017). In addition, the Markov approximation, as a stochastic treatment of the parabolic wave equation in random media (Sato 1989), is also used for analyzing peak delay and envelope broadening (e.g., Saito et al. 2002; Takahashi et al. 2009; Takahashi 2012). Furthermore, spatial variations of lithospheric heterogeneity have been globally established to correlate with tectonic settings based on Markov approximation (e.g., Kubanza et al. 2006, 2007). Besides the theoretical methods, numerical simulations of scattered waves propagating in random medium using finite difference methods have been conducted to determine the statistical parameters of random heterogeneities (e.g., Frankel and Clayton 1986; Yoshimoto et al. 2015; Emoto et al. 2017; Takemura et al. 2017) and effects on ground motions (e.g., Hartzell et al. 2010; Imperatori and Mai 2013; Savran and Olsen 2019). These studies have demonstrated various random models within the Earth's lithosphere and revealed significantly variable regional randomnesses from the shallow crust to uppermost mantle (Kubanza et al. 2007).

In this study, we analyze the teleseismic P wavefield including the coherent direct P-wave arrivals and following coda waves (Ritter et al. 1998). Coherent signals in the direct P waves are generated in the source region and propagate along the raypath between the source and receivers (Bannister et al. 1990). These signals are recorded showing similar waveforms at closely distributed seismic stations and can be used for localizing deterministic structural anomalies (Rothert and Ritter 2000). By contrast, the following incoherent coda waves, regarded as fluctuating wavefield, are generally generated by near-receiver scattering heterogeneities with sharp velocity and/or density contrasts in the lithosphere (Korn 1993). These incoherent coda waves can carry valuable information on fine-scale structures and provide a powerful tool for exploring average statistical properties of scattering regions beneath the stations (Ritter and Rothert 2000). In particular, modeling the temporal decay of coda wave amplitudes can further constrain the scattering parameters, such as the scattering strength and correlation length. The schematic illustration for the discipline is shown in Fig. 1.

Our study area is located in the northern part of Tien Shan. The Tien Shan region is known to be one of the most active intra-continental orogenic belts in the world caused by continent–continent convergence (Omuralieva et al. 2009). This orogenic belt consists of several east–west trending mountain ranges as well as intermountain basins (Lei and Zhao 2007; Li et al. 2016), displaying complex geologic and tectonic settings (Burtman 2015). Currently, the Tien Shan is experiencing an ongoing north–south crustal shortening due to the far-field India–Eurasia plate convergence. The crustal shortening rate is about 20 mm/year, which is nearly one half of the Indo-Eurasian convergence rate (Abdrakhmatov et al. 1996). Besides, the directions of crustal shortening are approximately in parallel with the north–south compressive stress axes (Ni 1978; Nelson et al. 1987). Therefore, the Tien Shan provides an ideal place for studying the mechanism of intra-continental mountain building and collision processes. During the last decade, numerous geophysical studies have been carried out for a better understanding of the mechanisms of regional geologic processes in this enigmatic region.

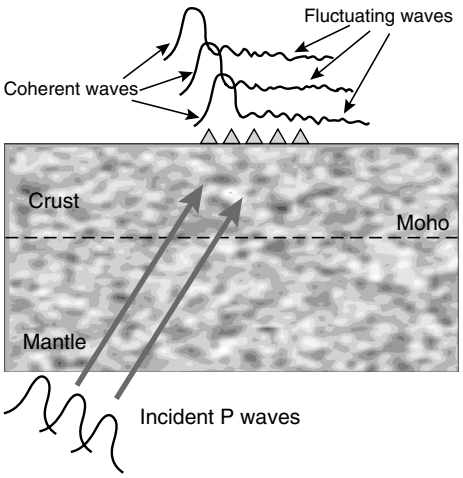

Fig. 1 A schematic illustration for the generation of teleseismic fluctuating waves. The incident primary P waves from teleseismic events are scattered off small-scale heterogeneities beneath the receivers during propagation through a random medium. The total waves recorded at the receivers consist of coherent and fluctuating waves

The velocity structure beneath this region is complicated by the presence of two underthrusting lithospheres imaged as high-velocity anomalies (Tarim Basin and Kazakh Shield) in tomographic models (e.g., Lei and Zhao 2007; Zabelina et al. 2013; Lü et al. 2019). Furthermore, tomographic studies have revealed prominent low seismic velocities in the upper mantle or even middle crust (e.g., Roecker et al. 1993; Li et al. 2009; Zabelina et al. 2013; Gilligan et al. 2014; Sychev et al. 2018) beneath the central Tien Shan. The low-velocity anomalies possibly

indicate a weak upper mantle (Gilligan et al. 2014) attributed to asthenospheric upwelling caused by lithospheric delamination (Lü et al. 2019). In addition, the presence of slow anomalies in the crust likely provides evidence for magmatic intrusion into the crust from the upper mantle. Therefore, the upwelling of mantle material may play a significant role in understanding the deep dynamic process and mechanism of mountain building (Li et al. 2016). However, by only analyzing coherent signals in the seismograms, these studies focus on tomographically resolved anomalies or sharp seismic discontinuities (e.g., Oreshin et al. 2002; Vinnik et al. 2004). Although some large-scale features of the crust and mantle have been revealed, the stochastic properties of finer-scale heterogeneities in the lithosphere of the northern Tien Shan are seldom investigated. Moreover, the relation between tomographically large-scale structures and random scattering heterogeneities underneath this region is still poorly understood. Characterization of these random fine-scale structures in the lithosphere would shed light on dynamic processes in the tectonically complicated Tien Shan region.

In this paper, we aim to investigate the averaged scattering characteristics of the lithosphere in the northern Tien Shan region using teleseismic P wavefield recorded by densely distributed stations. The teleseismic fluctuating wavefield method developed by Ritter et al. (1998) is adopted to deduce statistical parameters of the random media-type structures underneath the region. Then we model the envelope decay of the P-wave coda based on radiative transfer theory using a Monte Carlo simulation to further confine the scattering parameters. Our results reveal strong scattering with small correlation lengths in the whole crust or lithosphere beneath the study area.

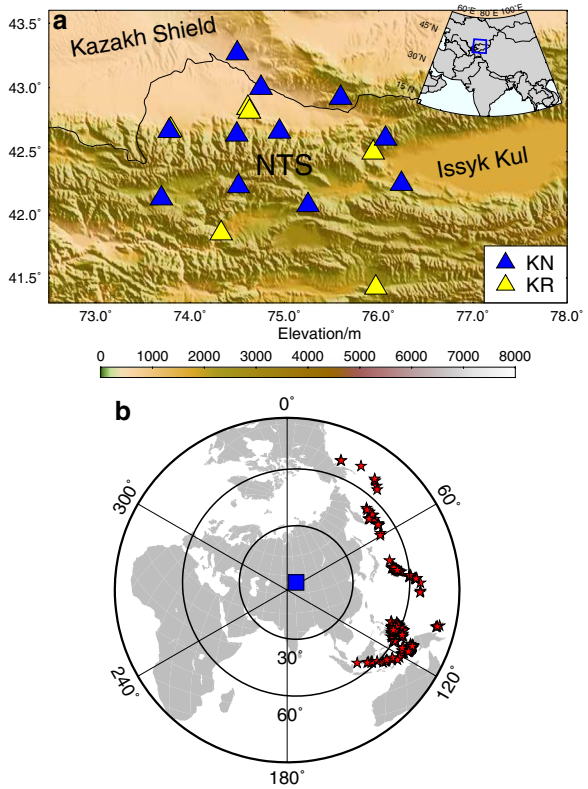

Fig. 2 **a** Map of the northern Tien Shan (NTS) region with the stations (triangles) from two networks KN (blue) and KR (yellow). The inset shows the geographic location of the study region (blue square). **b** Distribution of teleseismic events (red stars) used in this study. The square represents the study area

Data set

We select the vertical component waveforms at stations from two networks (KN: Kyrgyz Seismic Telemetry Network; KR: Kyrgyz Digital Network) in the northern Tien Shan (NTS) region. Specifically, 6 stations from the network KR and 11 from the network KN are used together. These stations are uniformly distributed in the study region (Fig. 2a), equipped with three-component broadband sensors (Roecker 2001) with the sampling rate of 40 Hz for KN network and 50 Hz for KR network, respectively. Due to the different sensor types in these two networks, all the waveforms are further deconvolved with instrument responses and resampled to 40 samples per second. Then we choose events based on the following criteria: (1) the focal depth should be larger than 110 km to exclude depth phases (e.g., pP, sP) earlier than 25 s after the direct P-wave based on Ak135 model (Kennett et al. 1995); (2) the epicentral distance is between 50° and 80° to ensure a nearly vertical incoming wave front; (3) simple and clear first-arrival P waves are required to avoid complex source processes. After filtering the data with a frequency band of 0.1–8.0 Hz, the waveforms with signal-to-noise ratio (SNR) less than 3 are further abandoned. The SNR is estimated by calculating the ratio of root-mean-square (RMS) amplitudes of teleseismic P-wave and noise 10 s before the P wave. This is to guarantee that the SNR is high enough to characterize the coda decay (Wang and Shearer 2017). Moreover, to obtain the average coherent wavefield, at least 8 recordings should be available for stable stacking results. The distribution for selected events with magnitude between 5.0 and 7.1 from 1994 to 2016 is displayed in Fig. 2b. The parameter information for all used events is listed in Additional file 1: Table S1.

Method

We use both teleseismic fluctuating wavefield method and Monte Carlo simulation approach to extract scattering parameters (the correlation length a and RMS

velocity contrast σ) of the random heterogeneity structure underneath the study area. It should be noted that in this study, we hypothetically ignore the scattering effects around the seismic source, since these effects may be weak compared to strong scattering in the lithosphere beneath the stations.

Teleseismic fluctuation wavefield method

To explore the scattering properties of a random medium, we use an approach called teleseismic fluctuation wavefield method (TFWM) (Ritter et al. 1998). This method assumes that the total wavefield (U_t) consists of the coherent wavefield (U_c) and fluctuating (incoherent) wavefield (U_f) after propagating through a random medium (Shapiro and Kneib 1993). We define ε as a measure of the wavefield fluctuations:

$$\left\langle \varepsilon^2 \right\rangle = \frac{\left\langle \left| U_f^2 \right| \right\rangle}{|\langle U_c \rangle|^2} = \frac{I_f}{I_c}, \tag{1}$$

where $\langle\rangle$ denotes a spatial averaging. I_f and I_c represent the fluctuating and coherent intensities (squared amplitude spectrum), respectively. By assuming a weak-fluctuating random medium with a Gaussian or exponential auto-correlation function (Sato 2019) as well as neglecting both backscattering and anelasticity effects, a relationship between $\langle\varepsilon^2\rangle$ and scattering parameters based on the Born approximation is derived (Ritter et al. 1998):

$$\left\langle \varepsilon^2 \right\rangle \approx \left[\exp\left(\frac{8\pi^2 L \sigma^2 a f^2}{v^2} \right) \right] - 1, \tag{2}$$

where L is the thickness of a scattering layer, f is the frequency and v is the average P velocity in a background model. σ and a are the RMS velocity perturbation and isotropic correlation length, respectively. This equation is only valid under the assumptions $ak\sigma^2 \ll 1$ as well as $ka \geq 1$ (k is the wavenumber) (Shapiro and Kneib 1993).

Then we take the natural logarithm of both sides in Eq. (2):

$$\ln\left(\left\langle \varepsilon^2 \right\rangle + 1 \right) = \frac{8\pi^2 L \sigma^2 a}{v^2} f^2 = \gamma f^2. \tag{3}$$

The structural parameter γ can be determined from a linear regression of left-handed side of Eq. (3) against f^2 by using the least-squares method. By applying (3) to all the events and stacking the frequency-dependent $\ln(\langle\varepsilon^2\rangle+1)$, we can reduce the effects from source time functions and obtain the averaged $\langle\gamma\rangle$ value. Then we can determine the parameter $a\sigma^2$ according to L/v^2 taken from previous studies.

Monte Carlo simulation

To solve the strong trade-offs in the scattering parameters, we model teleseismic P coda envelopes by using a Monte Carlo seismic phonon algorithm (Shearer and Earle 2004). This method is a powerful tool to simulate scattering processes and has been widely used in both regional and global studies (e.g., Margerin and Nolet 2003; Peng et al. 2008; Mancinelli and Shearer 2013; Wang and Shearer 2017). The details of this approach have been fully described in the previous paper (Shearer and Earle 2008). Here we only discuss some basic points.

This approach is based on the radiative transfer theory (Chandrasekhar 1960), which can describe the spatial–temporal distribution of energy of seismic wave in a scattering medium. In the simulation, the source radiates a large number of energy particles through the seismic velocity model based on ray theory. Whether a particle is scattered or not when hitting a scatterer is determined by the raypath length to a scatterer and scattering probabilities determined by random media models (Shearer and Earle 2004). As in previous studies, the random medium is generally characterized by power spectral density function (PSDF) type, the correlation length a, root-mean-square (RMS) fractional velocity fluctuation σ and decay order in large wavenumbers (Sato et al. 2012). During the propagation through the model, the energy of particles is reduced due to intrinsic attenuation. In final, the particles reaching the Earth surface are summed up as energy flux in time–distance bins.

For this study, we assume the scattering layer is described as a random medium characterized by an exponential auto-correlation function and the density versus velocity fluctuation scaling factor is 0.8 according to Birch's law (Birch 1961). Besides, the Q value is initially set to be 800 for the upper mantle. Since we only focus on random heterogeneity structures beneath the stations, we confine all the energy particles to propagate only downward from the source. In this way, we can in general avoid scattered energy from scattering in the lithosphere directly above the source.

Data analysis

We display an example of velocity seismograms from Event 2010.02.15.21.51 in Fig. 3. The total time window is chosen from 10 s before the direct P-wave arrival to about 25 s after the P-wave onset. The upper 12 traces (No. 1–12) show the original teleseismic P wavefield recordings representing the complete wavefield. We further normalize the waveforms to the maximum direct P waves. This normalization process could thus

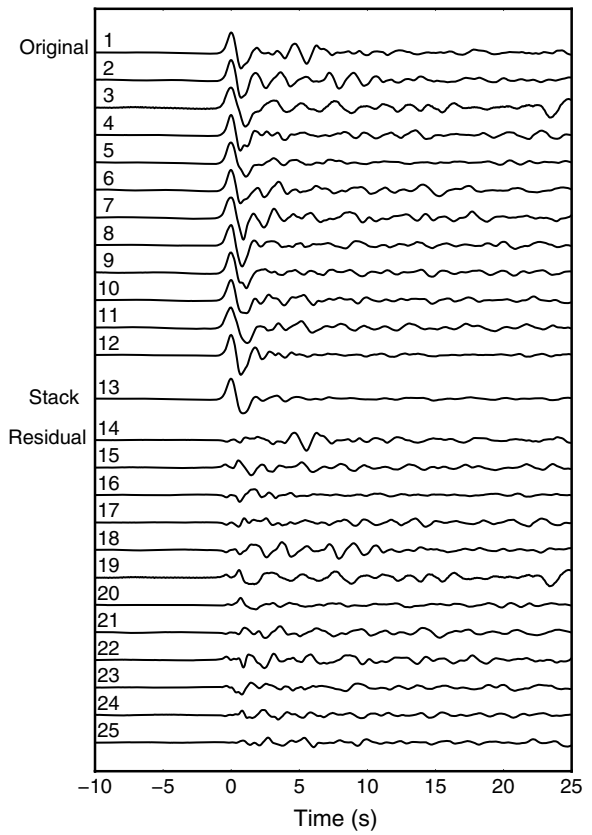

Fig. 3 Original velocity waveforms (complete wavefield) and residual waveforms (fluctuating wavefield) of Event 2010.02.15.21.51 (Lat: − 7.22, Lon: 128.72, Depth: 126.0 km). The single traces are time-shifted according to the first peak of direct P-wave and normalized to the individual maximum amplitudes. The stack in the middle represents the summed waveform from seismograms recorded by 12 stations in the NTS

reduce the site amplification effects beneath each individual station (Additional file 1: Fig. S1). Coda waves are clearly visible following the impulsive P wave. In addition, the coda amplitudes are much higher than the noise amplitudes before the P-wave onset. The coherent mean wavefield recorded at the array is shown in trace No. 13, resulting from the stack of the 12 individual waveforms (trace No. 1–12). This stacking procedure can enhance the coherent phases and suppress the scattered phases and noises significantly. Subsequently, the fluctuating wavefield represented by residual seismograms is obtained by subtracting the coherent wavefield (stacked waveform) from individual original recordings (complete wavefield). The subtraction procedure can thus remove signals that are generated in the source region and leave scattered signals behind. Besides, both stacking and subtracting processes can reduce the effects of source time function on the wavefield. The corresponding residual waveforms are shown in traces No. 14–25 with the same amplitude scale and in the order as traces No. 1–12. Compared with original recordings, the residual waveforms mostly contain amplitude fluctuations of scattered phases that are incoherent.

To test whether the later coherent teleseismic phases (e.g., PcP) would emerge in the fluctuating coda wavefield, we further apply the 3rd root stacking method (Muirhead and Datt 1976) to the original waveforms for each event in the vespagram analysis (Davies et al. 1971; Rost and Thomas 2002). An example for Event 2010.02.15.21.51 is shown in Fig. 4. The vespagram is calculated from 2.5 to 8.0 s/deg with a step of 0.1 s/deg. The maximum stacked energy for the P arrival is generated with a slowness value of 5.8 s/deg, whereas the theoretical one is 6.11 s/deg in the AK135 model (Kennett et al. 1995) for this event. The difference between the observed and theoretical P-wave slowness values could possibly be caused by heterogeneous structures beneath the stations. Except for the clearly visible P-wave energy, there are no other strong coherent signals in this vespagram. In addition, the PcP phase with a theoretical value of 4.23 s/deg in the AK135 model is not visible due to its weak amplitude. Therefore, the vespagram analysis demonstrates that the residual seismograms (fluctuating wavefield) in Fig. 3 (traces No. 14–25) mostly consist of incoherent, scattered waves, with the coherent phases being removed. We apply the same procedure to all the selected events and exclude events showing coherent non-direct P phases in the time window of interest. In total, we select 188 events for further analysis. Then the separation of coherent and fluctuating waveforms in the data is used for further extracting property parameters of random media beneath the receivers.

Results

Results from TFWM

We calculate the intensity of the coherent (I_c) and fluctuating (I_f) wavefield to obtain the ratio value $\langle \varepsilon^2 \rangle$ in the frequency domain. I_c is obtained by calculating the squared amplitude spectrum of the stacked waveform, whereas I_f is determined by stacking the amplitude spectrum of all residual waveforms. The plot is displayed in Fig. 5 for the event in Fig. 3. For frequencies lower than ~ 1.0 Hz, the intensity I_c is clearly larger than the intensity I_f (Fig. 5a). This means that the main energy of the incoming wavefield U_c is concentrated in this frequency range. However, for frequencies higher than about 1.5 Hz, the fluctuating wavefield dominates over the coherent wavefield. The logarithmic quotient $\langle \varepsilon^2 \rangle$ against frequency is shown in Fig. 5b. It can be observed that, from 0.3 to 2.5 Hz, the value $\ln(\varepsilon^2)$ increases continuously, implying the scattering intensity increases. However, for frequencies larger than 2.5 Hz, the value of $\ln(\varepsilon^2)$ remains almost constant,

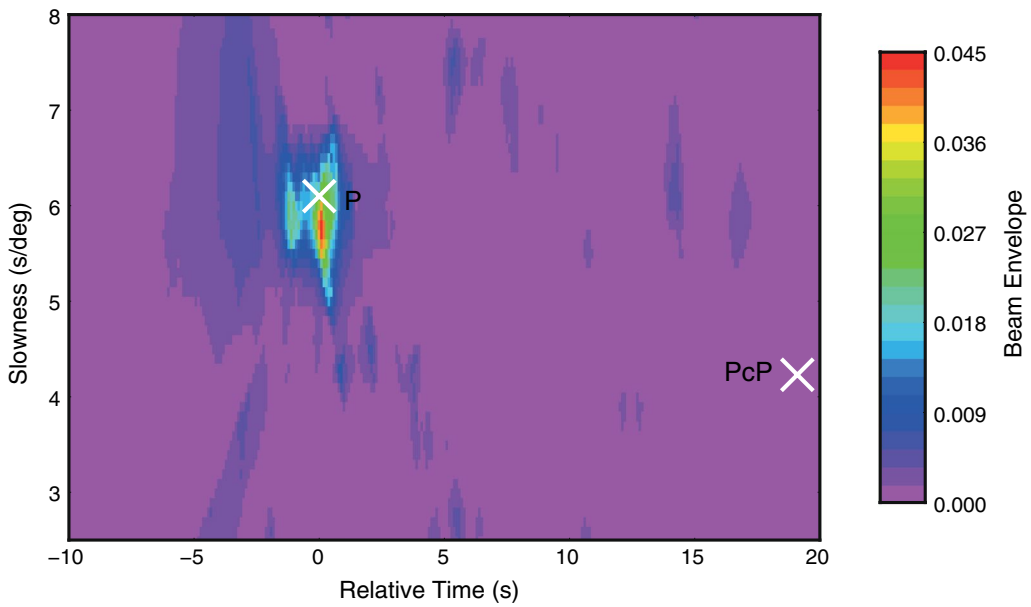

Fig. 4 Vespagrams of the original waveforms for Event 2010.02.15.21.51. A 3rd-root stacking is applied to the waveforms. The two white crosses denote the theoretical slowness values of P and PcP predicted by the AK135 model, respectively. Note that behind the strong direct P-wave energy, no other clear coherent arrivals are found within the analyzed time window (up to 25 s following the P arrival)

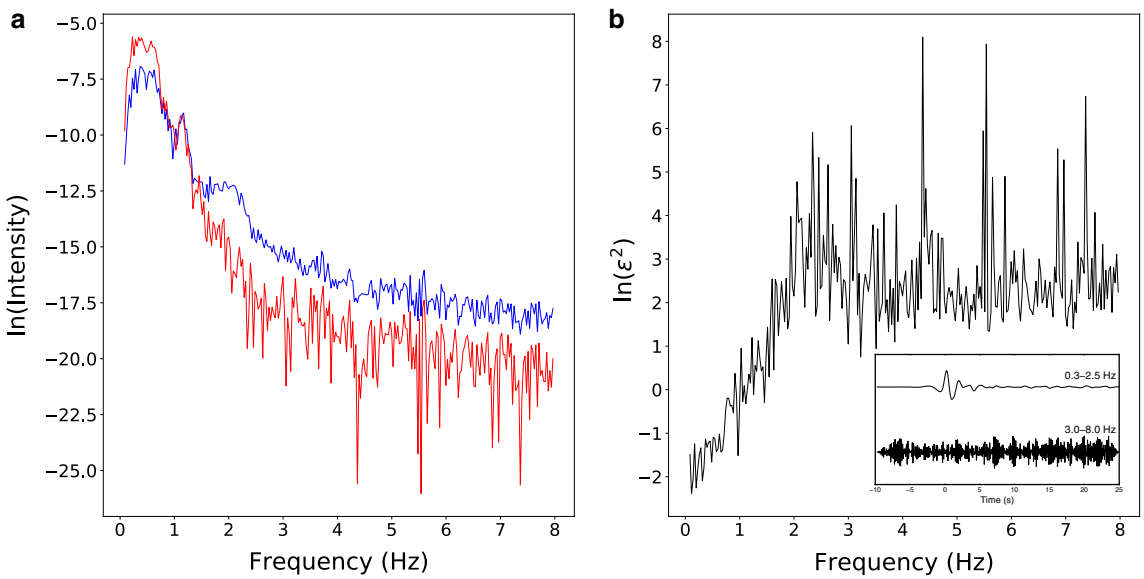

Fig. 5 **a** Plot of logarithm of squared amplitude spectra of the stacked (red) and residual (blue) waveforms for the event in Fig. 3. **b** Plot of logarithm of the ratio (ε^2) of fluctuating and coherent intensities against frequency

due to the intensity I_c reaching the level of the background noise (Ritter et al. 1998). This can be observed from the filtered seismograms in the bottom right corner of Fig. 5b. In the frequency band of 3.0–8.0 Hz, the coherent seismic signals are strongly contaminated by the background noise.

The similar feature of the frequency-dependent $\ln(\varepsilon^2)$ for all the events is presented in Fig. 6. The stacked curve represents the average properties of random structure beneath the stations in the NTS. We find that the value of $\ln(\varepsilon^2)$ is negative ($I_f < I_c$) below ~1.2 Hz, implying that the low-frequency content of teleseismic wavefield is

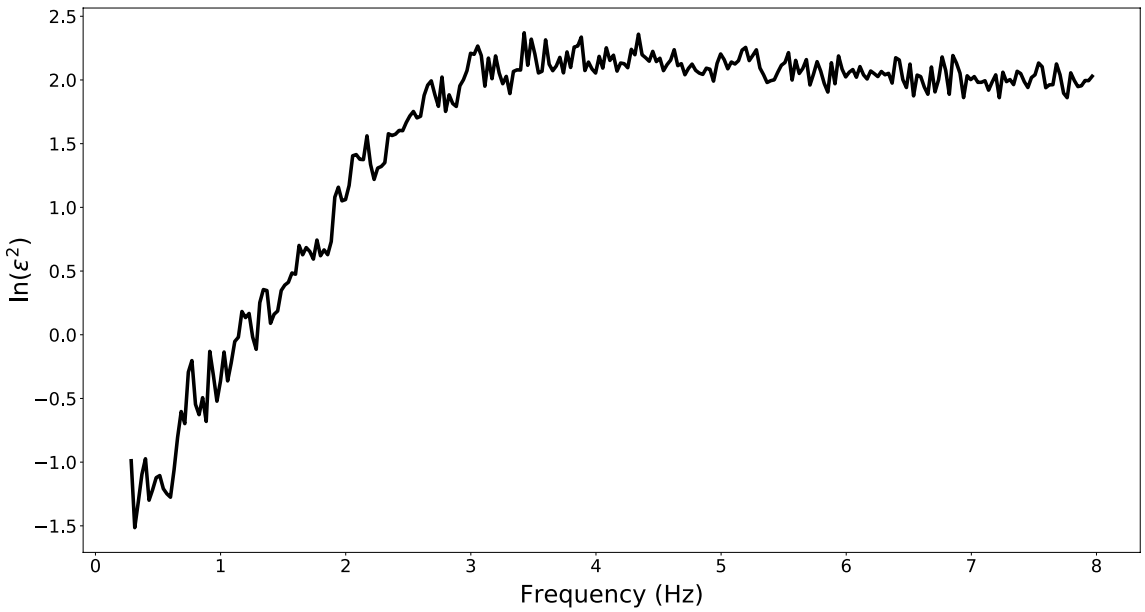

Fig. 6 Similar to Fig. 5, plot of logarithm of stack of ε^2 for all the analyzed events

mainly affected by relatively weak scattering (Ritter et al. 1998). In comparison, the $\ln(\varepsilon^2)$ value is positive between 1.2 and 3.0 Hz, indicating a gradually strong fluctuation regime in this frequency band. The relationship between the scattering strength and frequency possibly indicates the presence of multi-scale scattering heterogeneities. In addition, the frequency-dependent scattering strength is important for us to further understand the characteristic of seismic attenuation caused by scattering (Shapiro and Kneib 1993). This is, however, beyond the scope of this study.

We choose the frequency range of 0.3–2.5 Hz to determine the parameter γ using a quadratic least-squares fitting for Eq. (3). Figure 7 shows the fit of $\ln(\varepsilon^2+1)$ for the single event in Fig. 3 and fit of the stacked $\ln(\varepsilon^2+1)$ for all the events, respectively. The range of γ values for all events is between 0.16 and 0.67 Hz^{-2}, with an average of $\gamma = 0.37 \pm 0.12$ Hz^{-2}. In comparison, the averaged value $\langle\gamma\rangle$ derived from the stacked curves of $\ln(\varepsilon^2+1)$ against f^2 by the least-squares fit is 0.36 Hz^{-2} (Fig. 7b). The consistence of these two results and the small variation of γ indicate that the obtained parameter is very stable in the analysis.

The extreme and average values of γ are further used to estimate the scattering characteristics $\sigma^2 a$ according to the presumed quantity L/v^2 taken from previous studies (e.g., Roecker et al. 1993; Vinnik et al. 2004; Kumar et al. 2005). For this study region, we test four different scattering layers: $L = 15$ km, $L = 55$ km, $L = 75$ km and $L = 130$ km representing the upper crust, whole crust, lower lithosphere and whole lithosphere, respectively. The thicknesses and average velocities are listed in Table 1. We constrain the parameter σ to be less than 9%, considering that only small velocity perturbations are dominant in the lithosphere (Levander et al. 1994; Sobolev et al. 1997).

We display the curves of quantity $\sigma^2 a$ against L/v^2 in Fig. 8. The extreme values of $\gamma = 0.16$ and 0.67 Hz^{-2} are shown as two boundary curves to constrain the uncertainties of scattering parameters $\sigma^2 a$ for fixed L/v^2 values. For example, if the fluctuating waves following the direct P-wave are generated only in the whole crust ($L/v^2 = 1.3303$), then the quantity $\sigma^2 a$ ranges from 0.00152 to 0.00638. Supposing the velocity variation in the crust beneath the NTS is 5%, the isotropic correlation length is then between 0.6 and 2.5 km. We list a range of correlation lengths according to different RMS velocity perturbations for three γ values in Table 2. In this study, the wavenumber k is between 0.3 and 2.6 km^{-1}, given the seismic wavelength in our data ranges approximately from 2.4 to 24 km (corresponding to the frequency band 0.3–2.5 Hz). Since all the $\sigma^2 a$ values are less than 0.021 km, the condition $ak\sigma^2 \ll 1$ is thus satisfied and $ka \geq 1$ is valid if a is approximately larger than 0.8 km with the dominant frequency of about 1.5 Hz.

Results from envelope modeling

To further resolve the trade-offs for parameters a and σ, we model the temporal decay of the P-wave coda using the Monte Carlo simulation. We adopt the

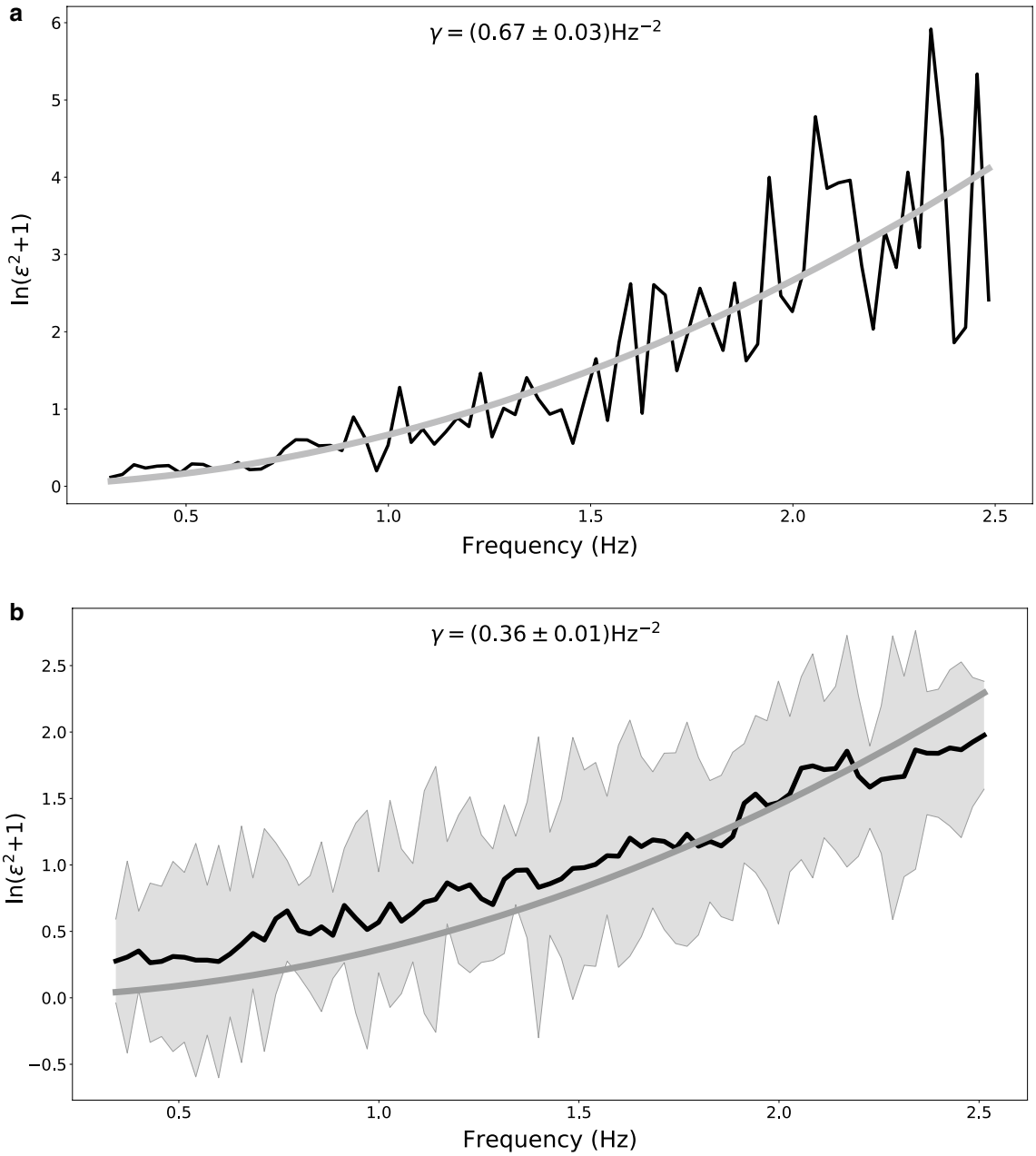

Fig. 7 Plot of $\ln(\varepsilon^2+1)$ against frequency for the determination of the parameter γ. The regression line (grey line) is derived from a quadratic least-squares fit of Eq. (3) in "Teleseismic fluctuation wavefield method" section. **a** Fit of $\ln(\varepsilon^2+1)$ versus frequency for Event 2010.02.15.21.51 with $\gamma = 0.67\ \mathrm{Hz}^{-2}$. **b** Fit of stacked $\ln(\varepsilon^2+1)$ for all the events with $\langle\gamma\rangle = 0.36\ \mathrm{Hz}^{-2}$. The grey area represents the interval of data stack with $\pm 1-\sigma$ error (σ denotes the standard error)

envelope-stacking method (e.g., Shearer and Earle 2008) to stack the data, which ignores the phase information and only considers the amplitude in the seismograms. Prior to stacking, the seismograms are further filtered at 0.3–2.5 Hz with a zero-phase third-order Butterworth filter. Envelopes of the seismograms are computed and aligned on the P-wave arrival and binned at 1.0° intervals in epicentral distance. The stacking process can further average out the focal mechanism effects by using many earthquakes. Thus we assume an isotropic point source at the 300 km depth for simplicity in our synthetic model. The frequency for synthetic model is set to 1.5 Hz, which

Table 1 Parameters of L/v^2 for four possible scattering layers beneath NTS

Scattering layer	Thickness L (km)	Average P-wave velocity v (km/s)	L/v^2 (s^2/km)
Upper crust	15	6.05	0.4098
Whole crust	55	6.43	1.3303
Lower lithosphere	75	8.01	1.1690
Whole lithosphere	130	7.34	2.4130

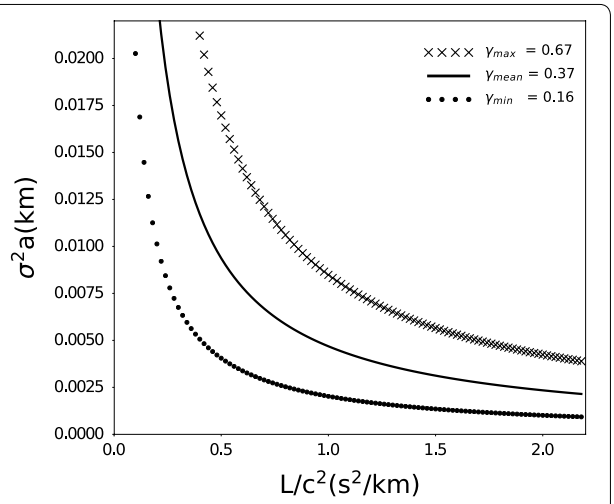

Fig. 8 Plot of the parameters $\sigma^2 a$ versus the quantity L/v^2 of the scattering layer for three γ values

is approximately the dominant frequency of the band-filtered data. We then model the stacked data according to the correlation lengths and RMS velocity perturbations in Table 2.

The comparisons between the stacked data and synthetics for four scattering layers are shown in Fig. 9. It can be seen in Table 2 that small velocity perturbations (1%) would result in large-size scattering heterogeneities that are huge compared with the scattering layer and unrealistic (Ritter et al. 1998). Therefore, we only calculate the synthetics for models with $\sigma = 3\%$, 5%, 7%, 9% and the corresponding a values. If the scattering is restricted only in the upper crust ($L = 15$ km), we find that synthetics from all upper crustal models cannot fit the stacked data. The amplitudes of scattered waves at short lapse times are all larger than those of the stacked data. The reason is probably that the mean free-path length (defined as inverse of total scattering coefficient in the inhomogeneous medium) is relatively large compared to the thin scattering layer. In such a case, the incident waves would interact with only a few scatterers, resulting in short-duration, but strong scattered wavefield. In comparison, for scattering existing in the whole crust ($L = 55$ km), the model with $\sigma = 9\%$ and $a = 0.4$ km can provide a reasonable fit to the stacked observations. A similar model ($\sigma = 9\%$ and $a = 0.5$ km) is found to match the stacked data, assuming the scattering is confined in the lower lithosphere ($L = 75$ km). In addition, if the scattering occurs in the whole lithosphere ($L = 130$ km), models with $\sigma = 7\%$ and $a = 0.4$ km can roughly fit the data stacks. In contrast, lithospheric scattering models with $\sigma = 9\%$ would underestimate the stacked data. Although the condition $ka \geq 1$ is not strictly satisfied if a is on the order of 0.4 km, we attribute this inconsistence to the Born approximation in the TFWM, whereas the Monte Carlo approach can accommodate multiple scattering naturally.

Table 2 Correlation lengths a for velocity perturbations $\sigma = 1$–9% for four different scattering layers taken from Table 1

Scattering layer	γ (Hz)	$\sigma^2 a$ (km)	$\sigma = 1\%$ a (km)	$\sigma = 3\%$ a (km)	$\sigma = 5\%$ a (km)	$\sigma = 7\%$ a (km)	$\sigma = 9\%$ a (km)
Upper crust	0.16	0.00494	49.4	5.5	2.0	1.0	0.6
	0.37	0.01144	114.4	12.7	4.6	2.3	1.4
	0.67	0.02071	207.1	23.0	8.3	4.2	2.6
Whole crust	0.16	0.00152	15.2	1.7	0.6	0.3	0.2
	0.37	0.00352	35.2	3.9	1.4	0.7	0.4
	0.67	0.00638	63.8	7.1	2.5	1.3	0.8
Lower lithosphere	0.16	0.00173	17.3	1.9	0.7	0.4	0.2
	0.37	0.00401	40.1	4.5	1.6	0.8	0.5
	0.67	0.00726	72.6	8.1	2.9	1.5	0.9
Lithosphere	0.16	0.00084	8.4	0.9	0.3	0.2	0.1
	0.37	0.00194	19.4	2.2	0.8	0.4	0.2
	0.67	0.00352	35.2	3.9	1.4	0.7	0.4

The boundary values of $\sigma^2 a$ are derived from the extreme values of γ

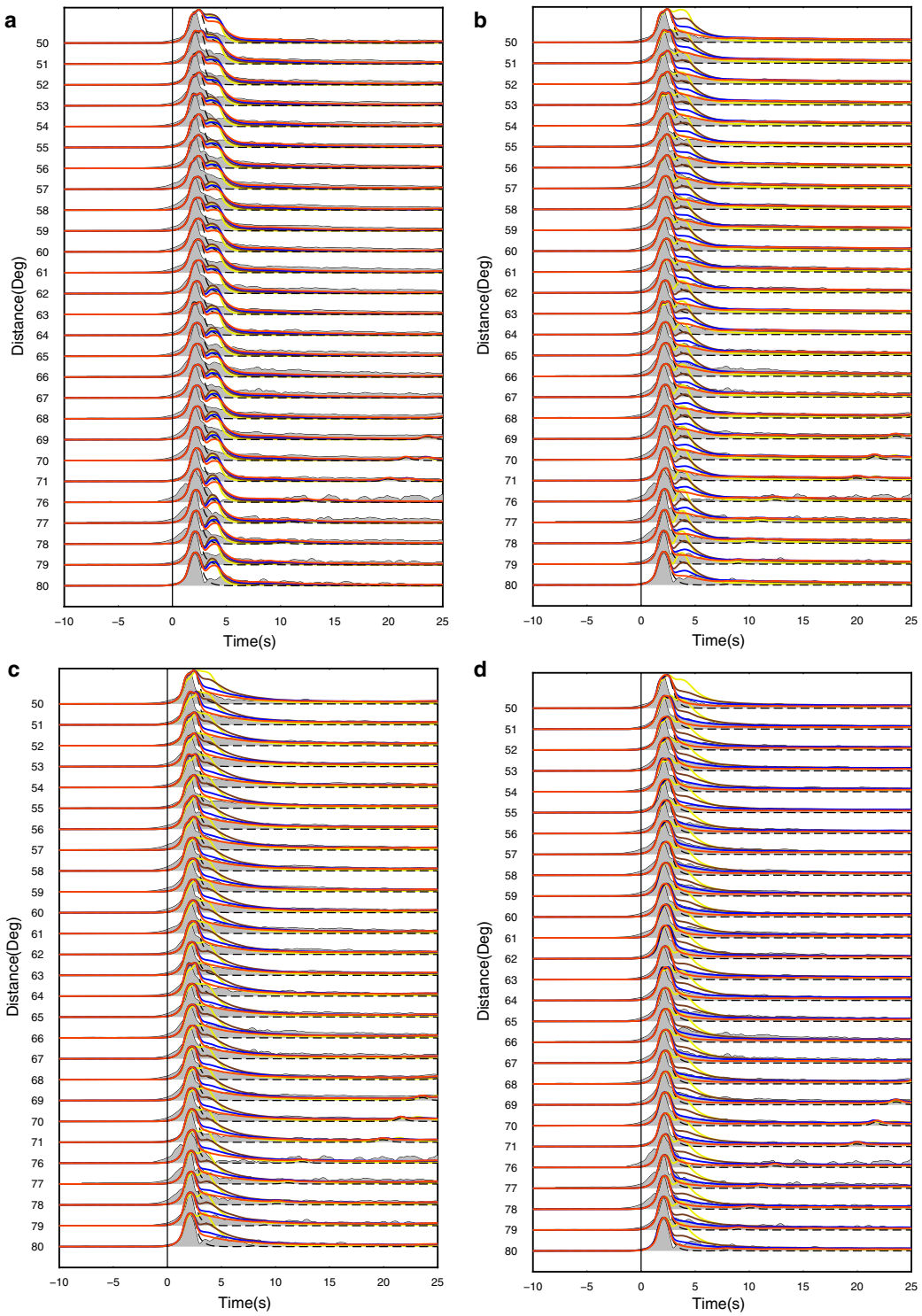

Fig. 9 Synthetics plotted against data stacks. The synthetics are generated by the Monte Carlo simulation for scattering models with different velocity variations and correlation lengths in the upper crust (**a**), whole crust (**b**), lower lithosphere (**c**) and whole lithosphere (**d**), respectively. The grey shading represents stacked data. The dashed lines denote the synthetics computed for the model without any scattering layers. In each column, the yellow, brown, blue and red lines represent the synthetics for models with RMS velocity perturbations (σ) of 3%, 5%, 7% and 9% as well as corresponding values of correlation lengths (a) in Table 2, respectively

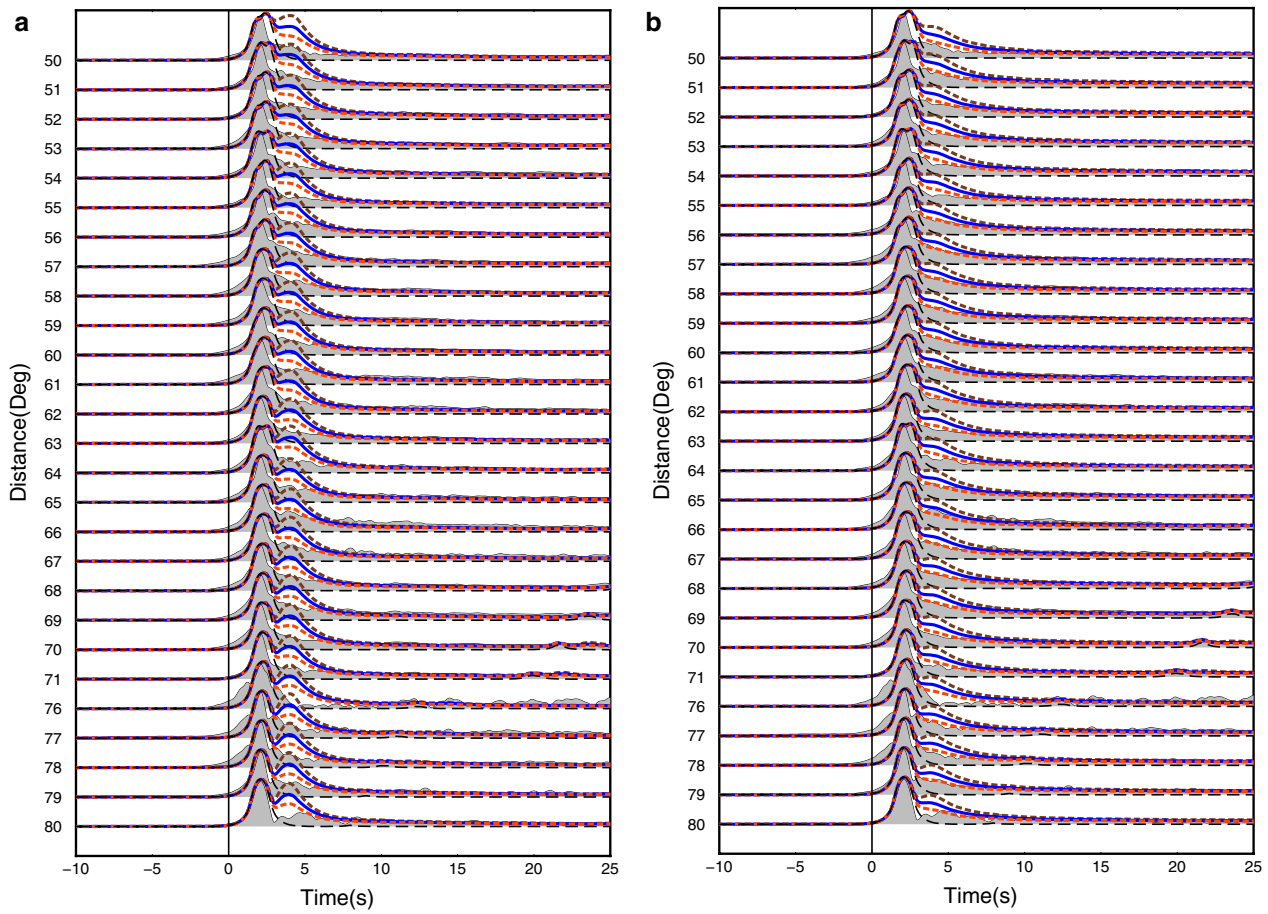

Fig. 10 Comparisons of synthetics for two scattering models with different frequency values (*f*). The blue lines represent synthetics with $f=1.5$ Hz while red and brown dashed lines represent synthetics with $f=1.2$ Hz and $f=1.8$ Hz, respectively. **a** The whole crustal scattering model with $\sigma=5\%$ and $a=1.4$ km. **b** The whole lithospheric scattering model with $\sigma=5\%$ and $a=0.8$ km

We note that scattering with different velocity contrasts and correlation lengths in two or more layers beneath the receivers can also explain the stacked wavefield fluctuations. Such models, however, cannot be determined uniquely by the above-mentioned TFWM. Moreover, it is impractical to perform a detailed grid search to perfectly model the data because there are such many free parameters to be constrained. Therefore, in this study, our main goal is to find model parameters obtained from TFWM that can produce a reasonable fit to the stacked observations.

Discussion

Factors affecting the simulations

Initially, we set the synthetic frequency value to be 1.5 Hz for the simulation. We notice that this frequency parameter can affect the P–P scattering coefficient in a very complicated way (see 4.64a in Sato et al. 2012), which changes the P coda envelope in our case. To test the effect of this factor on the synthetics, we run simulations for same scattering models using three different values of frequency and show the results in Fig. 10. The amplitudes of coda that is a few seconds later than the direct P waves increase with the frequency when the correlation length is on the order of ~ 0.4 km. Because the P–P scattering coefficient is fourth-power dependent on frequency, higher frequency values can result in larger amplitude of coda at short lapse times for teleseismic forward scattering. Future studies should involve studying the frequency-dependent relation for decay of coda wave.

Besides the frequency parameter, both the Q value and velocity–density variation ratio in the lithosphere are initially fixed in the simulation, we also need test how these two parameters would affect our preferred scattering models. Firstly, we simulate the P-wave coda envelope for different Q values in the upper mantle ($Q=800$ and 100). Results in Fig. 11a show that the damping by attenuation

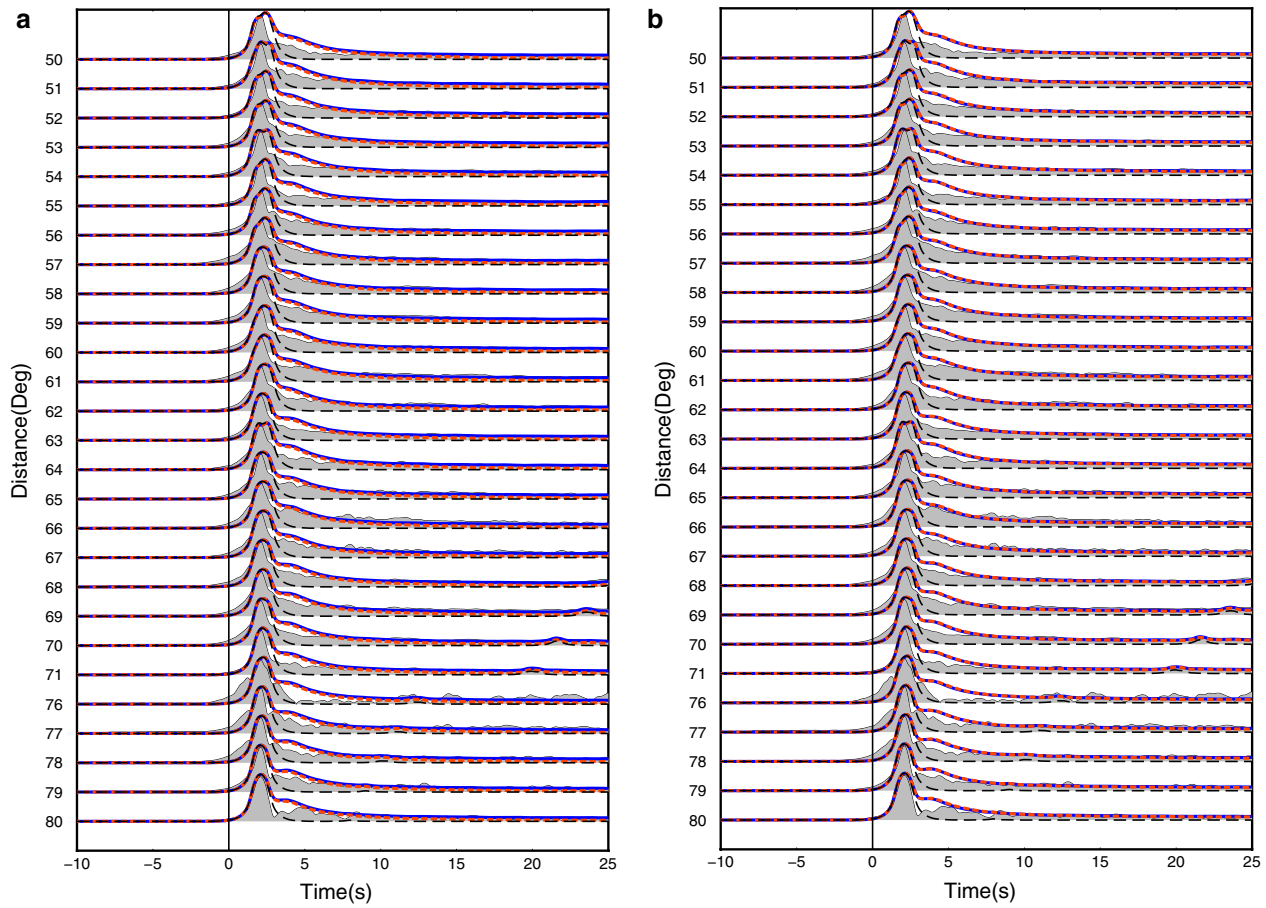

Fig. 11 A demonstration of how the parameters, attenuation (Q) and velocity-density variation scaling ratio (v), affect the P-wave coda synthetics. The scattering model is an exponential random medium with thickness of 130 km, correlation length of 0.8 km and RMS velocity perturbation of 5%. **a** Synthetics for models with $Q=100$ (dashed red lines) and $Q=800$ (blue lines) in the mantle, respectively. **b** Synthetics for models with $v=0$ (dashed red lines) and $v=0.8$ (blue lines), respectively

plays an insignificant role on the coda envelope. This is possibly due to the coda decay being dominated by the leaking of scattered energy into the lithosphere (Korn 1993). At the same time, this test confirms the assumption that anelasticity is negligible in the TFWM is valid. Secondly, we further test the effect of velocity–density variation scaling ratio on our synthetics. We recompute the synthetics for the scattering models with no density variations (the ratio value is 0) and find that the synthetics are not affected significantly (Fig. 11b). Because this ratio plays a major role in back-scattering (Mancinelli and Shearer 2013), while the P-wave coda in our case are mostly generated due to near-forward scattering.

Comparisons with previous scattering studies

The observations of teleseismic P coda in our data provide direct evidence for small-scale scattering heterogeneities in the northern Tien Shan region. We further compare the scattering properties of random heterogeneities beneath our study area with results in other regions over the globe using P-wave data. By analyzing the teleseismic P coda, Aki (1973) estimated the lithospheric heterogeneity to be ~4% with $a=10$ km at about 0.5 Hz in Montana. Using NORSAR array data, Flatté and Wu (1988) determined the statistical distribution of heterogeneities with RMS velocity variations of 1–4%. Similarly, random media with comparable RMS velocity variations are also detected in the southern California (Powell and Meltzer 1984) and southwestern Japan (Kobayashi et al. 2015; Emoto et al. 2017).

Based on the same TFWM, similar studies have revealed scattering heterogeneities with 1–7% P-wave velocity perturbations and correlation lengths ranging from 0.6 to 16 km in the whole crust or lithosphere of French Massif Central (Ritter et al. 1998), northern and central Europe (Hock et al. 2004), southwest Germany (Rothert and Ritter 2000), middle (Shen and Ritter 2010), northeast (Shen et al. 2010) and east China (Fan et al.

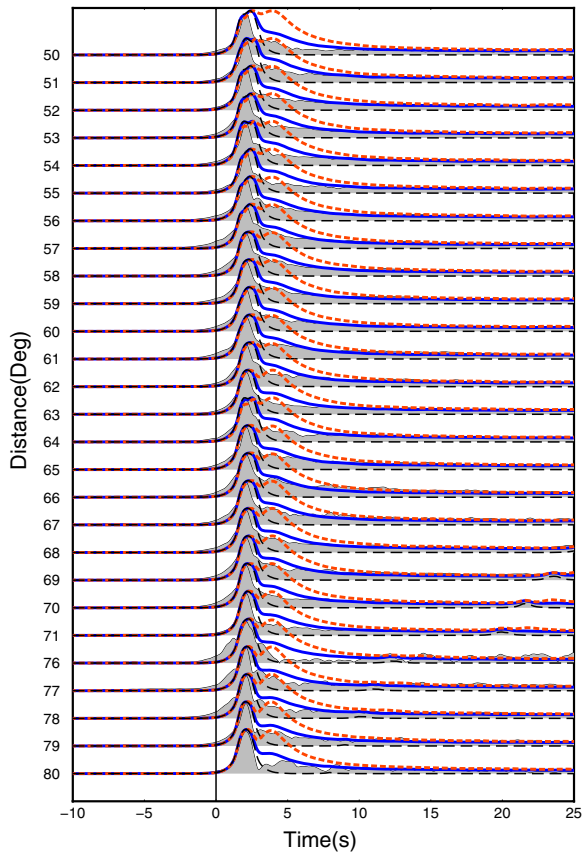

Fig. 12 A comparison of synthetics for similar scattering models to that in Fig. 11, but with $a = 1.5$ km (red) and $a = 0.8$ km (blue), respectively

2017). On a global basis, previous studies have further revealed significant regional variations in random heterogeneity of the lithosphere and the relation between the derived scattering parameters and the different geological structures (Kubanza et al. 2006). By assuming $a = 5$ km for all frequency bands, Kubanza et al. (2007) estimated σ to be 2–4% for random heterogeneities within the lithosphere in the stable continents while 5–10% in the tectonically active regions (e.g., island arcs, collision zones or subduction zones). These scattering heterogeneities in the lithosphere are proposed to originate from subducted oceanic crust or magmatic intrusions due to the related asthenospheric upwelling (Nishimura 2002; Rothert and Ritter 2000).

It should be noted that the value of correlation length a in our study is approximately the lowermost limit of previous results (also see Shearer 2015 for a review). Our simulations further show that models with larger values of a (e.g., 1.5 km) tend to over-predict amplitudes of P coda waves at small lapse times at all distances (Fig. 12). It thus suggests that the length scales of these random heterogeneities in the lithosphere are quite small (Wu and Aki 1985). Besides, the value of a in our study is generally comparable with isotropic (1.0 km) (e.g., Kobayashi et al. 2015; Yoshimoto et al. 2015) and vertical correlation length (0.5 km) (Tittgemeyer et al. 1996; Ryberg et al. 1995, 2000) inferred from modeling of P-wave scattering.

Small-scale scattering heterogeneities

Our preferred model for explaining the observed P-wave coda is a random medium characterized by an exponential auto-correlation function with a layer thickness of ~ 55 km $< L < 130$ km, RMS velocity perturbations of 6–9% and correlation lengths on the order of 0.4 km. The large values of RMS velocity perturbation σ indicate that there are very strong scattering heterogeneities in the whole crust or lithosphere beneath the northern Tien Shan, suggesting that this is a tectonically active region.

The strong scattering inhomogeneities beneath the northern Tien Shan are approximately located in prominent low-velocity zones in the middle-lower crust and upper mantle revealed by seismic tomography studies (e.g., Omuralieva et al. 2009; Sychev et al. 2018; Lü et al. 2019). Some of low-velocity anomalies can extend down to more than 150 km in the upper mantle (Roecker et al. 1993; Lei and Zhao 2007). The large P-wave velocity decrease in these anomalies could be likely caused by increased temperature, suggesting the existence of partial melting (Lei and Zhao 2007). A plausible explanation is that a small-scale convection or an intrusion of ascending hot mantle materials (e.g., Makeyava et al. 1992; Wolfe and Vernon 1998) are possibly trigged by the underthrusting of the Tarim and Kazakh lithosphere. Some segments of the thickened lithospheres can break off and sink into the deep mantle due to gravitational instability (Roecker et al. 1993; Lei and Zhao 2007). This would likely cause an upwelling mantle flow supplying a large amount of melts (Omuralieva et al. 2009). These melts would be formed in isolated pockets and show low resistivity in the upper mantle in the magnetotelluric study (Bielinski et al. 2003). The hot upwelling could be further confirmed by a thin mantle transition zone beneath the northern Tien Shan (Tian et al. 2010; Yu et al. 2017). A portion of these upwelling materials may further penetrate into the lithospheric mantle and lower crust to cause metasomatism as well as partial melting (Fig. 13). We speculate that such upwelling materials (melt pockets) are the origin of the strong small-scale velocity heterogeneities beneath the northern Tien Shan. Similarly, strong scattering heterogeneities (7–9%) within low-velocity zones are also proposed to be related with random distribution of fluids/melts supplied by the dehydration of subducting oceanic crust underneath Japan (Takahashi et al. 2009; Carcolé and Sato 2010; Takemura and Yoshimoto 2014). When teleseismic P waves

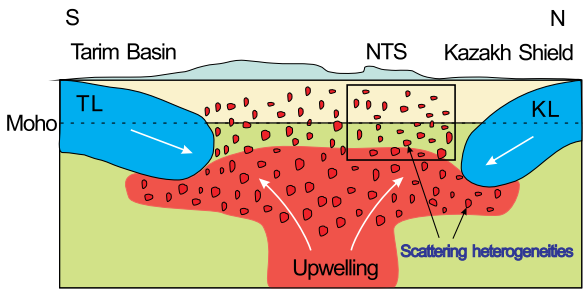

Fig. 13 A cartoon illustrating the small-scale melt pockets (small red patches) supplied from upwelling mantle materials beneath the northern Tien Shan (NTS). These melt pockets represent the scattering heterogeneities responsible for the fluctuating P-wave coda. The rectangle approximately denotes the scattering regions of interest beneath the study area. TL indicates the Tarim lithosphere and KL indicates the Kazakh lithosphere

propagate through the lithosphere beneath the NTS, these melt pockets functioning as small-scale scatterers can scatter the incident waves, generating the fluctuating P-wave coda in the observations. However, due to the small-scale lengths, tomography studies can only image clusters of melt pockets as low-velocity anomalies.

In the present study, we assume the scattering only exists above the lithospheric depth. However, we cannot exclude the possibility that the small-scale scattering heterogeneities in the mantle deeper than the lithosphere can also contribute to the P-wave coda. If this is the case, the scattering strength in the lithosphere would be weaker than the present results. Because the values of scattering thickness L cannot be obtained without knowledge from other studies, we can possibly optimize our results by combining results based on the energy-flux model where L can be roughly estimated (e.g., Korn 1997; Hock et al. 2004). Thus more seismic data containing three-component waveforms are needed to compare results from these two approaches. Although coda waves can be strongly excited by scattering due to surface topography (e.g., Imperatori and Mai 2015; Takemura et al. 2015; Hartzell et al. 2017), the relative contribution of topographic scattering in the high-frequency wavefield is only approximately 12% (Takemura et al. 2015) in local areas. However, scattering due to surface topography cannot be completely ruled out on generating the teleseismic P-wave coda, a more realistic numerical hybrid method (Monteiller et al. 2013) is needed to model these effects in the future research.

Conclusion

The teleseismic P wavefield provides a useful tool for characterizing the scattering properties beneath the stations. By using the P-wave coda from teleseismic events, we explore small-scale scattering heterogeneities underneath the northern Tien Shan. We obtain the statistical parameters of the random heterogeneities by analyzing the coherent and fluctuating P wavefield. To resolve the trade-offs in the scattering parameters, we further constrain the correlation lengths and velocity perturbations using the Monte Carlo simulation method. A crustal and/or lithospheric scattering model with velocity perturbations of 6–9% and isotropic correlation lengths on the order of 0.4 km is derived from the P-wave coda wavefield. The strong scattering is related with low-velocity anomalies in the lithosphere and likely to be hot upwelling asthenospheric materials in the form of melt pockets.

Supplementary information

Supplementary information accompanies this paper at https://doi.org/10.1186/s40623-020-1136-1.

Additional file 1: Table S1. Event information used in this study. **Figure S1.** Amplitude distribution for maximum teleseismic P-waves from all the events listed in Additional file 1: Table S1. The numerals in the horizontal axis are in correspondence to the numbers in the first column (Event No.) of Table S1. The absolute maximum values of P-wave amplitudes are shown in micron (μm).

Abbreviations

KN: Kyrgyz Seismic Telemetry Network; KR: Kyrgyz Digital Network; NTS: northern Tien Shan; PSDF: power spectral density function; RMS: root mean square; RTT: radiative transfer theory; SNR: signal-to-noise ratio; TFWM: teleseismic fluctuation wavefield method.

Acknowledgements

We would like to thank the editor Junichi Nakajima and two anonymous reviewers for their constructive comments to improve this manuscript. The present study is funded by the NSFC project (No. 41803034). We downloaded data from IRIS data repositories (NSF grant EAR-1261681). SAC (Goldstein and Snoke 2005) and ObsPy (Beyreuther et al. 2010) are used to analyze and process the seismograms. The figures are made using GMT5 (Wessel et al. 2013) and Matplotlib (Hunter 2007).

Authors' contributions

XM and ZH carried out the research. XM analyzed the seismic data and performed the simulation. XM and ZH wrote the manuscript. Both authors read and approved the final manuscript.

Funding

This study is supported by the NSFC project (No. 41803034) from National Natural Science Foundation of China.

Availability of data and materials

Teleseismic data supporting the results of the present paper are available through the Data Management Center (https://ds.iris.edu/ds/nodes/dmc/).

Ethics approval and consent to participate

Not applicable.

Consent for publication

Not applicable.

Competing interests

The authors declare that they have no competing interests.

Received: 7 November 2019 Accepted: 18 January 2020
Published online: 03 February 2020

References

Abdrakhmatov KY, Aldazhanov SA, Hager BH, Hamburger MW, Herring TA, Kalabaev KB, Makarov VI, Molnar P, Panasyuk SV, Prilepin MT, Reilinger RE, Sadybakasov IS, Souter BJ, Trapeznikov YA, Tsurkov VY, Zubovich AV (1996) Relatively recent construction of the Tien Shan inferred from GPS measurements of present-day crustal deformation rates. Nature 384:450–453

Aki K (1969) Analysis of the seismic coda of local earthquakes as scattered waves. J Geophys Res 74:615–631

Aki K (1973) Scattering of waves under the Montana Lasa. J Geophys Res 78:1334–1346

Aki K, Chouet B (1975) Origin of coda waves: source, attenuation, and scattering effects. J Geophys Res 80:3322–3342

Bannister SC, Husebye ES, Ruud BO (1990) Teleseismic P coda analysed by three-component and array techniques: deterministic location of topographic P-to-Rg scattering near the NORESS array. Bull Seismol Soc Am 80:1969–1986

Beyreuther M, Barsch R, Krischer L, Megies T, Behr Y, Wassermann J (2010) ObsPy: a python toolbox for seismology. Seismol Res Lett 81:530–533

Bielinski RA, Park SK, Rybin A, Batalev V, Jun S, Sears C (2003) Lithospheric heterogeneity in the Kyrgyz Tien Shan imaged by magnetotelluric studies. Geophys Res Lett 30:1806

Birch F (1961) Composition of the earth's mantle. Geophys J R Astron Soc 4:295–311

Burtman VS (2015) Tectonics and geodynamics of the Tian Shan in the Middle and Late Paleozoic. Geotectonics 49:302–319

Carcolé E, Sato H (2010) Spatial distribution of scattering loss and intrinsic absorption of short-period S waves in the lithosphere of Japan on the basis of the Multiple Lapse Time Window Analysis of Hi-net data. Geophys J Int 180:268–290

Chandrasekhar S (1960) Radiative Transfer. Dover, New York

Davies D, Kelly EJ, Filson JR (1971) Vespa process for analysis of seismic signals. Nat Phys Sci 232:8–13

Emoto K, Sato H (2018) Statistical characteristics of scattered waves in three-dimensional random media: comparison of the finite difference simulation and statistical methods. Geophys J Int 215:585–599

Emoto K, Saito T, Shiomi K (2017) Statistical parameters of random heterogeneity estimated by analysing coda waves based on finite difference method. Geophys J Int 211:1575–1584

Eulenfeld T, Wegler U (2017) Crustal intrinsic and scattering attenuation of high-frequency shear waves in the contiguous United States. J Geophys Res Solid Earth 122:4676–4690

Fan X-P, He Y-C, Wang J-F, Yang Y (2017) Crust seismic scattering strength below the middle-south segment of Tancheng-Lujiang fault zone. Chin J Geophys 60:244–253

Flatté SM, Wu R-S (1988) Small-scale structure in the lithosphere and asthenosphere deduced from arrival time and amplitude fluctuations at NORSAR. J Geophys Res 93:6601–6614

Frankel A, Clayton RW (1986) Finite difference simulations of seismic scattering: implications for the propagation of short-period seismic waves in the crust and models of crustal heterogeneity. J Geophys Res 91:6465–6489

French SW, Romanowicz B (2015) Broad plumes rooted at the base of the Earth's mantle beneath major hotspots. Nature 525:95–99

Gaebler PJ, Eulenfeld T, Wegler U (2015) Seismic scattering and absorption parameters in the W-Bohemia/Vogtland region from elastic and acoustic radiative transfer theory. Geophys J Int 203:1471–1481

Gilligan A, Roecker SW, Priestley KF, Nunn C (2014) Shear velocity model for the Kyrgyz Tien Shan from joint inversion of receiver function and surface wave data. Geophys J Int 199:480–498

Goldstein P, Snoke A (2005) "SAC Availability for the IRIS Community". Incorporated Institutions for Seismology Data Management Center Electronic Newsletter

Gusev AA, Abubakirov IR (1999) Vertical profile of effective turbidity reconstructed from broadening of incoherent body-wave pulses-II. Application to Kamchatka data. Geophys J Int 136:309–323

Hartzell S, Harmsen S, Frankel A (2010) Effects of 3D random correlated velocity perturbations on predicted ground motions. Bull Seismol Soc Am 100:1415–1426

Hartzell S, Ramírez-Guzmán L, Meremonte M, Leeds A (2017) Ground motion in the presence of complex topography II: earthquake sources and 3D simulations. Bull Seismol Soc Am 107:344–358

Hock S, Korn M, Ritter JRR, Rothert E (2004) Mapping random lithospheric heterogeneities in northern and central Europe. Geophys J Int 157:251–264

Hunter JD (2007) Matplotlib: a 2D graphics environment. Comput Sci Eng 9:90–95

Imperatori W, Mai PM (2013) Broad-band near-field ground motion simulations in 3-dimensional scattering media. Geophys J Int 192:725–744

Imperatori W, Mai PM (2015) The role of topography and lateral velocity heterogeneities on near-source scattering and ground-motion variability. Geophys J Int 202:2163–2181

Kennett BLN, Engdahl ER, Buland R (1995) Constraints on seismic velocities in the Earth from travel times. Geophys J Int 122:108–124

Kobayashi M, Takemura S, Yoshimoto K (2015) Frequency and distance changes in the apparent P-wave radiation pattern: effects of seismic wave scattering in the crust inferred from dense seismic observations and numerical simulations. Geophys J Int 202:1895–1907

Korn M (1993) Determination of site-dependent scattering Q from P-wave coda analysis with an energy-flux model. Geophys J Int 113:54–72

Korn M (1997) Modelling the teleseismic P coda envelope: depth dependent scattering and deterministic structure. Phys Earth Planet Int 104:23–36

Kubanza M, Nishimura T, Sato H (2006) Spatial variation of lithospheric heterogeneity on the globe as revealed from transverse amplitudes of short-period teleseismic P-waves. Earth Planets Space 58:45–48. https://doi.org/10.1186/BF03352618

Kubanza M, Nishimura T, Sato H (2007) Evaluation of strength of heterogeneity in the lithosphere from peak amplitude analyses of teleseismic short-period vector P waves. Geophys J Int 171:390–398

Kumar P, Yuan X, Kind R, Kosarev G (2005) The lithosphere–asthenosphere boundary in the Tien Shan-Karakoram region from S receiver functions: evidence for continental subduction. Geophys Res Lett 32:L07305

Lai Y, Chen L, Wang T, Zhan Z (2019) Mantle transition zone structure beneath Northeast Asia from 2-D triplicated waveform modeling: implication for a segmented stagnant slab. J Geophys Res Solid Earth 124:1871–1888

Lei J, Zhao D (2007) Teleseismic P wave tomography and the upper mantle structure of the central Tien Shan orogenic belt. Phys Earth Planet Inter 162:165–185

Levander A, Hobbs RW, Smith SK, England RW, Snyder DB, Holliger K (1994) The crust as a heterogeneous 'optical' medium, or 'crocodiles in the mist'. Tectonophysics 232:281–297

Li Y, Shi L, Gao J (2016) Lithospheric structure across the central Tien Shan constrained by gravity anomalies and joint inversions of receiver function and Rayleigh wave dispersion. J Asian Earth Sci 124:191–203

Li Z, Roecker S, Li Z, Wei B, Wang H, Schelochkov G, Bragin V (2009) Tomographic image of the crust and upper mantle beneath the western Tien Shan from the MANAS broadband deployment: Possible evidence for lithospheric delamination. Tectonophysics 477:49–57

Lü Z, Gao H, Lei J, Yang X, Rathnayaka S, Li C (2019) Crustal and upper mantle structure of the Tien Shan orogenic belt from full-wave ambient noise tomography. J Geophys Res Solid Earth 124:3987–4000

Ma X, Sun X, Thomas C (2019) Localized ultra-low velocity zones at the eastern boundary of Pacific LLSVP. Earth Planet Sci Lett 507:40–49

Makeyava I, Vinnik L, Roecker S (1992) Shear-wave splitting and small-scale convection in the continental upper mantle. Nature 358:144–147

Mancinelli NJ, Shearer PM (2013) Reconciling discrepancies among estimates of small-scale mantle heterogeneity from PKP precursors. Geophys J Int 195:1721–1729

Margerin L, Nolet G (2003) Multiple scattering of high-frequency seismic waves in the deep earth: modeling and numerical examples. J Geophys Res 108(B5):2234

Monteiller V, Chevrot S, Komatitsch D, Fuji N (2013) A hybrid method to compute short-period synthetic seismograms of teleseismic body waves in a 3-D regional model. Geophys J Int 192:230–247

Muirhead KJ, Datt R (1976) The Nth root process applied to seismic array data. Geophys J R Astron Soc 47:197–210

Nelson MR, McCaffrey R, Molnar P (1987) Source parameters for 11 earthquakes in the Tien Shan, central Asia, determined by P and SH waveform inversion. J Geophys Res 92:12629–12648

Ni J (1978) Contemporary tectonics in the Tien Shan region. Earth Planet Sci Lett 41:347–354

Nishimura T (2002) Spatial distribution of lateral heterogeneity in the upper mantle around the western Pacific region as inferred from analysis of transverse components of teleseismic P-coda. Geophys Res Lett 29:52-1–52-4

Omuralieva A, Nakajima J, Hasegawa A (2009) Three-dimensional seismic velocity structure of the crust beneath the central Tien Shan, Kyrgyzstan:

implications for large- and small-scale mountain building. Tectonophysics 465:30–44
Oreshin S, Vinnik L, Peregoudov D, Roecker S (2002) Lithosphere and asthenosphere of the Tien Shan imaged by S receiver functions. Geophys Res Lett 29:1191
Peng Z, Koper KD, Vidale JE, Leyton F, Shearer P (2008) Inner-core fine-scale structure from scattered waves recorded by LASA. J Geophys Res 113:B09312
Powell CA, Meltzer AS (1984) Scattering of P-waves beneath SCARLET in southern California. Geophys Res Lett 11:481–484
Ritter J, Rothert E (2000) Variations of the lithospheric seismic scattering strength below the Massif Central, France and the Frankonian Jura, SE Germany. Tectonophysics 328:297–305
Ritter JRR, Shapiro SA, Schechinger B (1998) Scattering parameters of the lithosphere below the Massif Central, France, from teleseismic wavefield records. Geophys J Int 134:187–198
Roecker S (2001) Constraints on the crust and upper mantle of the Kyrgyz Tien Shan from the preliminary analysis of GHENGIS broad-band data. Russ Geol Geophys 42:1554–1565
Roecker SW, Sabitova TM, Vinnik LP, Burmakov YA, Golvanov MI, Mamatkanova R, Munirova L (1993) Three-dimensional elastic wave velocity structure of the western and central Tien Shan. J Geophys Res 98:15779–15795
Rost S, Thomas C (2002) Array seismology: methods and applications. Rev Geophys 40:1–27
Rothert E, Ritter JRR (2000) Small-scale heterogeneities below the Graefenberg array, Germany, from seismic wavefield fluctuations of Hindu Kush events. Geophys J Int 140:175–184
Ryberg T, Fuchs K, Egorkin V, Solodilov L (1995) Observation of high-frequency teleseismic Pn waves on the long-range Quartz profile across northern Eurasia. J Geophys Res 100:18151–18163
Ryberg T, Tittgemeyer M, Wenzel F (2000) Finite difference modeling of P-wave scattering in the upper mantle. Geophys J Int 141:787–800
Saito T, Sato H, Ohtake M (2002) Envelope broadening of spherically outgoing waves in three-dimensional random media having power-law spectra. J Geophys Res 107:1
Sato H (1989) Broadening of seismogram envelopes in the randomly inhomogeneous lithosphere based on the parabolic approximation: southeastern Honshu, Japan. J Geophys Res 94:17735–17747
Sato H (2019) Power spectra of random heterogeneities in the solid earth. Solid Earth 10:275–292
Sato H, Emoto K (2018) Synthesis of a scalar wavelet intensity propagating through von Kármán-type random media: radiative transfer theory using the Born and phase-screen approximations. Geophys J Int 215:909–923
Sato H, Fehler MC, Maeda T (2012) Seismic Wave Propagation and Scattering in the Heterogeneous Earth. Springer, New York
Savran WH, Olsen KB (2019) Ground motion simulation and validation of the 2008 Chino Hills earthquake in scattering media. Geophys J Int 219:1836–1850
Scherbaum F, Sato H (1991) Inversion of full seismogram envelopes based on the parabolic approximation: estimation of randomness and attenuation in southeast Honshu, Japan. J Geophys Res 96:2223–2232
Shapiro SA, Kneib G (1993) Seismic attenuation by scattering: theory and numerical results. Geophys J Int 114:373–391
Shearer PM (2015) Deep earth structure: seismic scattering in the deep earth. In: Schubert G (ed) Treatise on geophysics, 2nd edn. Elsevier BV, Amsterdam, pp 759–787
Shearer PM, Earle PS (2004) The global short-period wavefield modelled with a Monte Carlo seismic phonon method. Geophys J Int 158:1103–1117
Shearer PM, Earle PS (2008) Observing and modeling elastic scattering in the deep earth. Adv Geophys 50:167–193
Shen X-Z, Ritter JRR (2010) Small-scale heterogeneities below the Lanzhou CTBTO seismic array, from seismic wave field fluctuations. J Seismol 14:481–493
Shen X-Z, Zhang S-Z, Zheng Z, Hao C-Y (2010) Study on the small-scale heterogeneities below the Hailaer CTBTO seismic array. Chin J Geophys 53:1158–1166 **(in Chinese with English abstract)**
Sobolev SV, Zeyen H, Granet M, Achauer U, Bauer C, Werling F, Altherr R, Fuchs K (1997) Upper mantle temperatures and lithosphere-asthenosphere system beneath the French Massif Central constrained by seismic, gravity, petrologic and thermal observations. Tectonophysics 275:143–164
Sychev IV, Koulakov I, Sycheva NA, Koptev A, Medved I, El Khrepy S, Al-Arifi N (2018) Collisional processes in the crust of the northern Tien Shan inferred from velocity and attenuation tomography studies. J Geophys Res Solid Earth 123:1752–1769
Takahashi T (2012) Three-dimensional attenuation structure of intrinsic absorption and wide-angle scattering of S waves in northeastern Japan. Geophys J Int 189:1667–1680
Takahashi T, Sato H, Nishimura T, Obara K (2009) Tomographic inversion of the peak delay times to reveal random velocity fluctuations in the lithosphere: method and application to northeastern Japan. Geophys J Int 178:1437–1455
Takemura S, Yoshimoto K (2014) Strong seismic wave scattering in the low-velocity anomaly associated with subduction of oceanic plate. Geophys J Int 197:1016–1032
Takemura S, Furumura T, Maeda T (2015) Scattering of high-frequency seismic waves caused by irregular surface topography and small-scale velocity inhomogeneity. Geophys J Int 201:459–474
Takemura S, Kobayashi M, Yoshimoto K (2017) High-frequency seismic wave propagation within the heterogeneous crust: effects of seismic scattering and intrinsic attenuation on ground motion modelling. Geophys J Int 210:1806–1822
Tian X, Zhao D, Zhang H, Tian Y, Zhang ZJ (2010) Mantle transition zone topography and structure beneath the central Tien Shan orogenic belt. J Geophys Res 115:B10308
Tittgemeyer MF, Wenzel F, Fuchs K, Ryberg T (1996) Wave propagation in a multiple-scattering upper mantle: observations and modeling. Geophys J Int 127:492–502
Tkalčić H, Young MK, Muir JB, Davies R, Mattesini M (2015) Strong, multi-scale heterogeneity in earth's lowermost mantle. Sci Rep 5:18416
Vinnik LP, Reigber C, Aleshin IM, Kosarev GL, Kaban MK, Oreshin SI, Roecker SW (2004) Receiver function tomography of the central Tien Shan. Earth Planet Sci Lett 225:131–146
Wang W, Shearer PM (2017) Using direct and coda wave envelopes to resolve the scattering and intrinsic attenuation structure of Southern California. J Geophys Res Solid Earth 122:7236–7251
Wegler U, Korn M, Przybilla J (2006) Modeling full seismogram envelopes using radiative transfer theory with Born scattering coefficients. Pure Appl Geophys 163:503–531
Wessel P, Smith WHF, Scharroo R, Luis J, Wobbe F (2013) Generic mapping tools: improved version released. EOS Trans Am Geophys Union 94:409–410
Wolfe C, Vernon F (1998) Shear-wave splitting at central Tien Shan: evidence for rapid variation of anisotropic patterns. Geophys Res Lett 25:1217–1220
Wu R-S (1985) Multiple scattering and energy transfer of seismic waves separation of scattering effect from intrinsic attenuation I. Theoretical modelling. Geophys J Int 82:57–80
Wu R, Aki K (1985) Elastic wave scattering by a random medium and the small-scale inhomogeneities in the lithosphere. J Geophys Res 90:10261–10273
Yoshimoto K, Takemura S, Kobayashi M (2015) Application of scattering theory to P-wave amplitude fluctuations in the crust. Earth Planets Space 67:199. https://doi.org/10.1186/s40623-015-0366-0
Yu Y, Zhao D, Lei J (2017) Mantle transition zone discontinuities beneath the Tien Shan. Geophys J Int 211:80–92
Zabelina IV, Koulakov IYu, Buslov MM (2013) Deep mechanisms in the Kyrgyz Tien Shan orogen (from results of seismic tomography). Russ Geol Geophys 54:695–706
Zeng Y, Su F, Aki K (1991) Scattering wave energy propagation in a random isotropic scattering medium: 1. Theory. J Geophys Res 96:607–619

Publisher's Note